



**HAL**  
open science

## **In-situ 3D X-ray investigation of ceramic powder sintering at the particle length-scale**

Aatreya Manjulagiri Venkatesh, Didier Bouvard, Pierre Lhuissier, Julie Villanova, Cyril Rajon

► **To cite this version:**

Aatreya Manjulagiri Venkatesh, Didier Bouvard, Pierre Lhuissier, Julie Villanova, Cyril Rajon. In-situ 3D X-ray investigation of ceramic powder sintering at the particle length-scale. *Ceramics International*, 2024, 50 (3), pp.4715-4728. 10.1016/j.ceramint.2023.11.216 . hal-04311320

**HAL Id: hal-04311320**

**<https://hal.science/hal-04311320>**

Submitted on 28 Nov 2023

**HAL** is a multi-disciplinary open access archive for the deposit and dissemination of scientific research documents, whether they are published or not. The documents may come from teaching and research institutions in France or abroad, or from public or private research centers.

L'archive ouverte pluridisciplinaire **HAL**, est destinée au dépôt et à la diffusion de documents scientifiques de niveau recherche, publiés ou non, émanant des établissements d'enseignement et de recherche français ou étrangers, des laboratoires publics ou privés.

# In-situ 3D X-ray investigation of ceramic powder sintering at the particle length-scale

Aatreya Manjulagiri Venkatesh <sup>a</sup>, Didier Bouvard <sup>b</sup>, Pierre Lhuissier <sup>c</sup>, Julie Villanova <sup>d</sup>, Cyril Rajon <sup>e</sup>

<sup>a</sup> Univ. Grenoble Alpes, CNRS, Grenoble INP, SIMAP, 38000 Grenoble, France, [mvaatreya@gmail.com](mailto:mvaatreya@gmail.com)

<sup>b</sup> Univ. Grenoble Alpes, CNRS, Grenoble INP, SIMAP, 38000 Grenoble, France, [didier.bouvard@grenoble-inp.fr](mailto:didier.bouvard@grenoble-inp.fr)

<sup>c</sup> Univ. Grenoble Alpes, CNRS, Grenoble INP, SIMAP, 38000 Grenoble, France, [pierre.lhuissier@simap.grenoble-inp.fr](mailto:pierre.lhuissier@simap.grenoble-inp.fr)

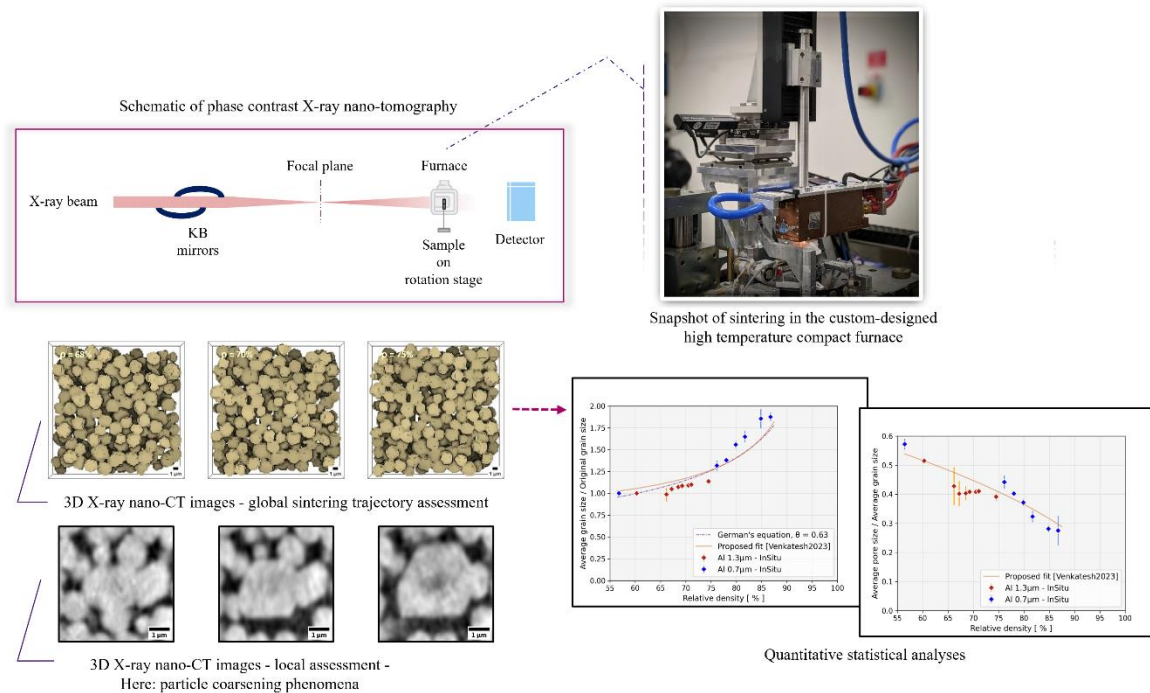
<sup>d</sup> ESRF - The European Synchrotron, 71 Avenue des Martyrs, 38000 Grenoble, France, [julie.villanova@esrf.fr](mailto:julie.villanova@esrf.fr)

<sup>e</sup> Univ. Grenoble Alpes, CNRS, Grenoble INP, SIMAP, 38000 Grenoble, France, [cyril.rajon@simap.grenoble-inp.fr](mailto:cyril.rajon@simap.grenoble-inp.fr)

## Abstract

We report an in-situ investigation of a high-temperature ceramic powder sintering performed for the first time at the particle length-scale. This was made possible by the phase-contrast X-ray nano-holotomography technique at the ID16B nano-analysis beamline of the European Synchrotron Radiation Facility (ESRF), featuring nanometer resolution (25 nm) capabilities. To perform sintering inside the synchrotron hutch, a compact high-temperature furnace was designed and developed. The sequence of real-time 3D images captured the collective behavior of the particles as well as the local-level specificities. A list of sintering indicators corresponding to the evolution of the particle shape, particle size, inter-particle neck size, pore size and pore curvature were extracted. The effect of these parameters on densification and their influence on the overall microstructural development were analyzed. Our results demonstrate the potential of synchrotron-based X-ray nano-tomography for studying complex sintering phenomena in 3D.

## Graphical abstract



## Keywords

Sintering; Ceramic powders; Synchrotron X-ray nano-tomography; In-situ investigation; High-temperature compact furnace; Quantitative image analysis; Pore curvature.

## 1.1 Introduction

The properties and performance of sintered materials are reflective of their microstructural evolution during sintering. This evolution is in turn driven by the thermodynamics and the kinetics of the sintering mechanisms [1] [2] [3] [4] [5]. Studying these mechanisms would in essence be best possible by looking not just at the macroscopic conduct, as in, by dilatometry etc., but rather by a real-time monitoring of the microstructural development in the course of sintering. A complete grasp on the intrinsic microstructure is therefore vital for a comprehensive study of sintering.

For ceramic materials, considering that sintering is the main fabrication route, the progress achieved with respect to microstructural inspection is not yet adequate. Reasons for this being - the complex architecture of the ceramic particles, their small (micron or sub-micron) size, their tendency to agglomerate, the ensuing limitations on the experimental set-ups to address

these concerns and moreover, the difficulties encountered in the subsequent imaging context. As far as we are aware, no three-dimensional (3D) in-situ examination on ceramic sintering at the particle length-scale has been performed so far. A direct access to the 3D morphology of a particle as a whole could provide us with comprehensive information about its associated arrangement, behavior and interaction with other sets of particles. This could then help us cast light on still-unresolved aspects of ceramic sintering such as particle rearrangement, evolution of the shape of particles and pores, coupling of densification with grain growth, etc.

In the early 2000s, with the onset of the usage of X-ray tomography in material science, substantial advancements leading to 3D visualization in metallic sintering at the local particle scale were carried out, especially using synchrotron facilities [6] [7] [8] [9]. Simultaneously, Bernard *et al.* [10] were the first ones to deploy micro-computed tomography on sintered ceramic samples. Same sets of grains on pre-sintered samples were observed in 3D at the micrometer scale in an ex-situ framework. Baruchel *et al.* [11], in their collection of studies on X-ray tomography, illustrated the various prospects offered by the techniques in a ceramic sintering setting. They were optimistic about the forthcoming breakthroughs in the field of synchrotron X-ray sources, enabling nano-range capabilities. Furthermore, Upadhyaya *et al.* highlighted the decisive benefits offered by 3D imaging over 2D from a practical viewpoint [12]. The importance of 3D input data in modeling an ever-more accurate description of the sintering evolution was stressed upon by Exner [13].

Around the 2010s, exploring the synchrotron X-ray resources available at that time, Xu *et al.* achieved preliminary success at observing a packing of boron carbide powder in-situ during isothermal sintering. Studies were performed on the porosity evolution and the material migration between the grains in their successive works [14] and [15]. The experimental findings were found to be consistent with conventional sintering theories. Likewise, three distinct stages of sintering in alumina samples were observed and distinguished, together with a few associated phenomena from the reconstructed 3D images by Xu *et al.* [16]. The same research group further went on to qualitatively rationalize the observed 3D image results in silicon carbide particles sintering.

Nevertheless, as the spatial resolution capabilities at the synchrotron sources at the time were not fine enough to capture intricate local details, the aforementioned studies on ceramic sintering were all conducted only at an agglomerate level.

Although, of late, considerable progress has been achieved on that front. Villanova *et al.* have developed a fast in-situ nano-tomography (nano-CT) apparatus at the European Synchrotron Radiation Facility (ESRF) [17], presenting a combination of previously unheard-of pixel size (few nanometers) and acquisition speed (few tens of seconds). This tomography configuration was applied to report for the first time, an assessment of the neck curvature development during the glass-sintering process. Subsequently, nano-CT advances in other synchrotron facilities worldwide have since found applications, for example, an attempt at monitoring the high-temperature sintering of SiC/TiO<sub>2</sub> [18], in detecting detailed 3D morphology of defects developed during alumina sintering [19], and in examining the origin of the defects and the microstructural evolution during the sintering of multi-layer ceramic capacitors [20] [21].

More recently, taking advantage of the nano-CT route, our research group managed to carry out sintering observations on micron-sized alumina samples at the nano-scale [22]. These post-mortem experiments were undertaken at the ESRF with an unprecedented resolution of 25 nm pixel size, enabling the detection of the particle and the pore phases with ease. Classical sintering parameters were both qualitatively and quantitatively analyzed.

However, the post-mortem experiments provide only the final state of the sintered material corresponding to a specific time or temperature, without revealing the intermediate and dynamic changes in the process. A proper follow-up of the sintering parameters over time cannot be done, and a thorough understanding of the heterogenic behavior in the material, if present, is not possible.

The aim of the present work is to go beyond the limitations of the above-mentioned work and to have an even deeper exploration in the X-ray nano-CT domain during the sintering process. A successful attempt was made to track alumina sintering in-situ, in 3 dimensions, at the same super-high resolution of 25 nm, and encompassing different stages of sintering. A high temperature compact furnace was designed, developed, and integrated into the X-ray nano-tomography set-up at the nano-imaging beamline of the ESRF for the same. These are the first set of high-temperature in-situ experiments to be accomplished at this length-scale on ceramic powders, offering a visual confirmation of a sintering cycle. Tackling open questions on the mechanisms and kinetics of ceramic sintering, while capturing the collective behavior taking place during a sintering process should now be feasible. Accordingly, here, key parameters governing sintering such as the inter-particle neck size, grain size, pore size etc. have been monitored over time. In addition, it was possible to take a closer look at the same set of image

sections at a local level to find the existence of non-uniformity, if any. Making use of the local observations, an analysis is conducted on the evolution in the shape of the grains in the early stages of sintering. Also, with the real-time data, the sintering process is classified into different stages based on the evolution of their pore curvatures.

## 1.2 Materials and Methods

### 1.2.1 Sample preparation

The two alumina powders considered for the in-situ investigation are from Sumitomo Chemical Co., Ltd.'s advanced alumina series – AA-07 and AA-1.3 respectively. The manufacturers claim the powders to be of superior characteristics, having high purity, uniformity, precisely controlled particle size distribution and almost-rounded polyhedral shapes [23]. The corresponding average particle sizes of the two powders were around 0.7  $\mu\text{m}$  and 1.3  $\mu\text{m}$  (**Figure 1**), which are compatible with the resolution achievable in the synchrotron set-up. The two powders sinter at 1500°C, as evident from the preliminary dilatometry trials conducted.

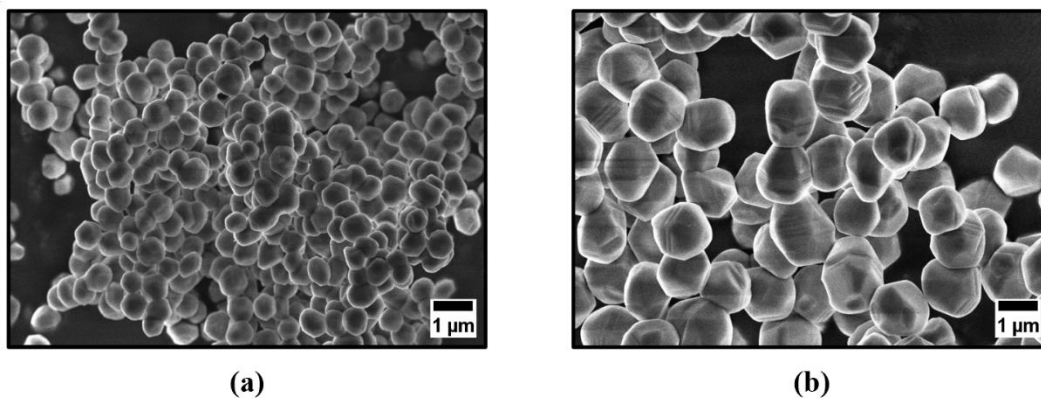


**Figure 1. SEM (scanning electron microscopy) images of the chosen alumina powders with average particle sizes of around (a) 0.7  $\mu\text{m}$  and (b) 1.3  $\mu\text{m}$  respectively.**

The powders were subjected to die compaction to instill mechanical strength enough to attain a relative density of ~60%. These samples were further broken into tiny fragments of ~100  $\mu\text{m}$  in diameter and ~1 mm in height, so as to allow imaging of a significant number of grains under the field of view expected. The fragments were attached on to an alumina rod using a ceramic glue, to be placed on the sample holder in the synchrotron beamline and to be later introduced into the furnace.

## 1.2.2 Furnace - design and development

We report a high temperature compact furnace specially designed and developed (in coordination with *CERHEC, Paris*) for the in-situ studies. Extending the scope of the technique presented by Villanova *et al.* [17], the unique characteristics of the furnace open new possibilities across domains requiring this particular synchrotron investigation. The major attribute of the furnace is its ability to reach higher temperatures (1500°C) rapidly, while withstanding it for a very long duration (~50 hours for this experiment), with barely any fluctuations. It is compact and compatible with other accessories present in the synchrotron beamline. Its functioning complies with the restrictions in the beamline hutch, especially with regard to the ambient temperature and the radiation.

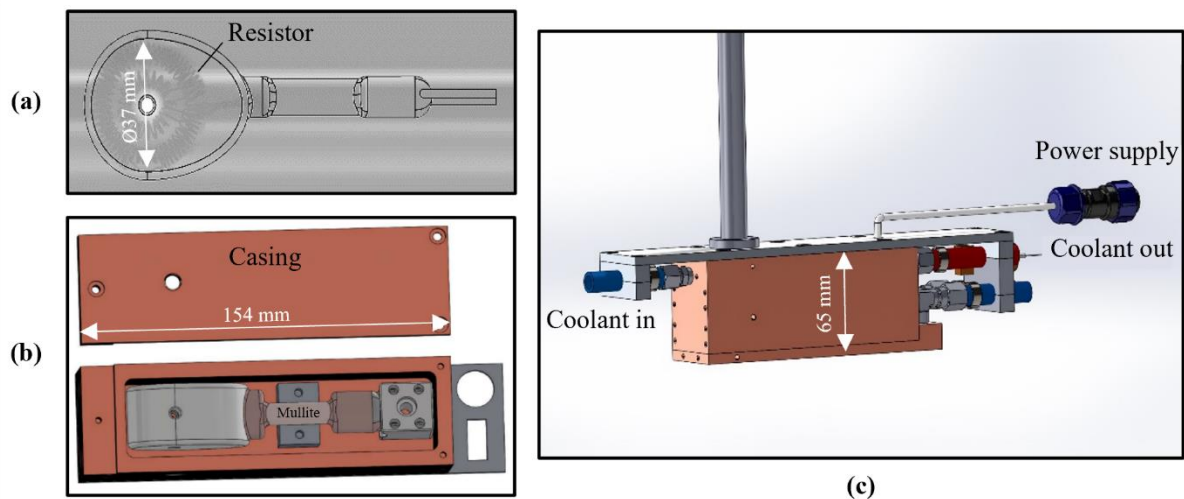


**Figure 2.** (a) Internal design of the furnace resistor, imaged from a laboratory tomography source (*EasyTom XL by RX-Solutions*), (b) components of the furnace system inside the casing, assembled together to set up the (c) cooling system.

Taking inspiration from the research work of Guinebretière *et al.* [24], a platinum resistor which meets the temperature requirements was used as the heating element. The internal arrangement ( $\text{Ø}37$  mm) of the coils can be seen in **Figure 2** (a), providing a homogenous heating in the chamber. The resistor is wrapped in an insulating ceramic foam, with a hole in the center for beam transmission. The system is held by an arm, made of mullite (possessing lower thermal expansion properties), which is further connected to an external power supply. (**Figure 2** (b)). The components were then placed inside a casing made of copper, specially devised for an effective cooling of the system (**Figure 2** (c)). The coolant branches into 8 channels, giving a continuous surge in full flow. This constant circulation maintains the outer surface temperature of the system efficiently during the course of the experiment. This is

critical as even slight fluctuations in the temperature would have an impact on the focusing system in the hutch, which would lead to a change in the size of the source and consequently affect the nano-resolution of the images. The entire assembly is 65 mm in height and 154 mm in length. The architecture also has provisions to introduce the sample, for the X-rays to pass through, and for the insertion of the thermocouple meant for temperature measurement. The DC power supply (*delta electronica*) was set to a voltage of 42.7 V to achieve and sustain the specified temperature.

### 1.2.3 Synchrotron X-ray nano-tomography experiment

Isothermal sintering treatments and X-ray nano-tomography measurements were performed on the alumina samples at the nano-analysis beamline ID16B of the ESRF [25]. The beamline presents a phase-contrast X-ray holotomography system, its state-of-the-art being introduced in Villanova *et al.* [17] and the general applicability of which, especially in material science, are detailed in Mayo *et al.* [26] and Cloetens *et al.* [27].

Please refer to Venkatesh *et al.* [22] for the details on the set-up as the configuration of the experiment remained the same here (**Figure 3**). Images were acquired via 4-distance imaging. 3203 projections with a pixel size of 25nm (field of view of  $64*64*54 \mu\text{m}^3$ ) were collected over  $360^\circ$  using an X-ray incoming beam with an energy of 29.53 keV.

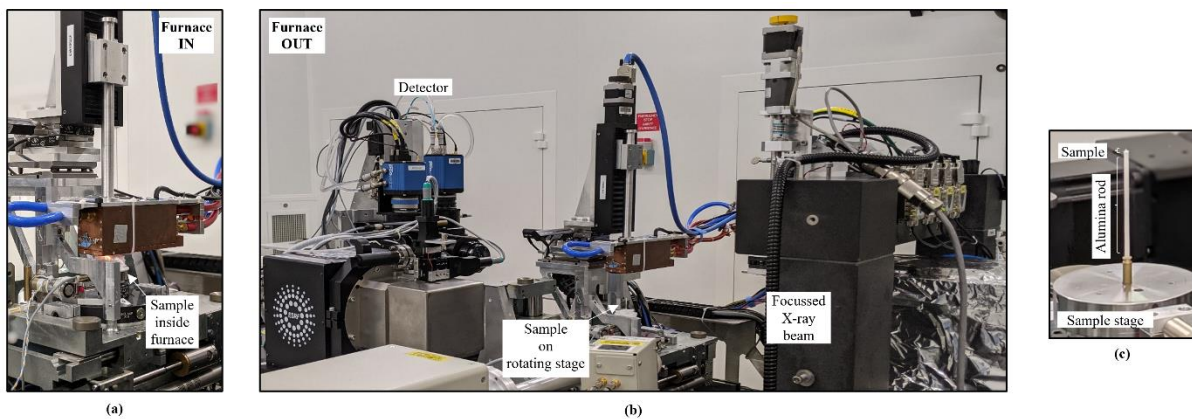


**Figure 3. Stages in the X-ray nano-CT imaging: (a) heating of the furnace with the sample inside and (b) launching of holo-tomography with the furnace out of the sample. (c) Depiction of the sample placed on the rotating holder.**

The alumina sample was mounted on the sample holder (**Figure 3** (c)) and aligned with the detector. The furnace was arranged in such a way that it could be moved down for the sample to be placed inside it and later taken out, as and when required (**Figure 3** (a) (b)). Thanks to

this mounting, holo-tomography could be performed with the furnace above the sample at all times, without having to dismount the sample or the furnace. This guarantees that the same area of the sample gets imaged through the experiment.

The parameters of the acquisition were validated in Venkatesh *et al.* [22], with 4-distance imaging taking ~20 min of time while achieving a resolution high enough to detect fine details in the alumina microstructure. Here, as the sample would have drastically evolved in that period of ~20 min, the scan time was not compatible vis-à-vis the sintering kinetics for a continuous in-situ investigation. Any changes in the acquisition parameters ran a risk of degradation in the resolution obtained. As a trade-off, in-situ trials in an interrupted manner were preferred to a continuous acquisition.

As in **Figure 3** (a), isothermal heating was secured with the furnace moving down on the sample for pre-defined times. After each time-step, the furnace was taken out of the sample (**Figure 3** (b)), to initiate and carry out the imaging process. The X-rays passed through the sample to be recorded by the detector system. The microstructure was expected to be frozen for that period.

The entire process was automatized and controlled from outside the beamline hutch. Accordingly, the furnace was powered from an external source and the temperature was maintained at 1500°C throughout the experiment. The thermocouple in the furnace was earlier calibrated with a eutectic (Ni 23.2 wt% Nb - 1282°C) to determine the current temperature of the sample. A recirculating cooler FL1203 (procured from *Julabo GmbH*), filled with an ethylene glycol coolant, clubbed with the effective casing design of the furnace ensured that the temperature just outside the surface of the furnace system was ~23°C, which is the regulated ambient temperature of the beamline hutch. Following the imaging, phase-retrieval based on the contrast transfer function (CTF) was carried out in an iterative fashion. Tomographic reconstruction followed by means of the ESRF PyHST2 software package [28], rendering the 3D distribution of the sample.

#### **1.2.4 Image processing and segmentation**

##### ***Ring removal***

To deal with the so-called ring artefacts visible on the reconstructed volumes, a method which works on the phase-retrieved radiographs that store the information of the 2D projections, was attempted here. Errors, if present in the radiographs, later appear as rings on the reconstructed

volume. Defective detector elements, dust from the insulating wool etc., could be the plausible reasons for the same as listed out in [29] and [30].

A blend of Double flat field correction, Munch correction and Dering correction were imposed on the radiographs. The principle underlying these methods and the corresponding parameters involved are explained elsewhere [29]–[31]. Particularly, in Munch correction, the range of Fourier and wavelet filters were tweaked on a trial-and-error basis for adjusting the ring correction levels. A visual assessment confirmed that this approach improved the quality of the reconstructed images.

Image-filtering prescribed in Lyckegaard *et al.* [32], using a MATLAB script, worked well in the case of post-mortem experiments for the same samples in Venkatesh *et al.* [22]. This script, which targets the reconstructed volume and filters them, proved unsuccessful here at removing the rings completely.

### ***Image registration and correlation***

A look at the processed reconstructed volumes at different time-steps revealed misalignments (shifts and rotations) in the imaged area between the respective image states, combined with a global evolution of the sample during sintering. A manual correlation was too demanding and toolkits for image correlation provided by SPAM software were used to solve this issue [33] [34], as detailed in section 1 of *Supplementary Information*.

However, the large data size (2560\*2560\*2160 pixels) of the reconstructed images proved to be a constraint in SPAM. Only a few Z-slices at a time were hence considered. They were further cropped into smaller volumes of interest (VOIs) of 520\*3 voxels for the following image treatment and quantitative measurements.

### Segmentation methodology

Synchronized image states, once obtained, are to be subjected to pre-processing operations prior to computing quantitative analyses. The image treatment was carried out in Avizo software package [35] and consisted of the following workflow, as shown for one of the cropped image stacks of the reconstructed alumina 1.3  $\mu\text{m}$  in **Figure 4**. The instruction manual of Avizo has a detailed explanation of the methodologies and their corresponding parameters.

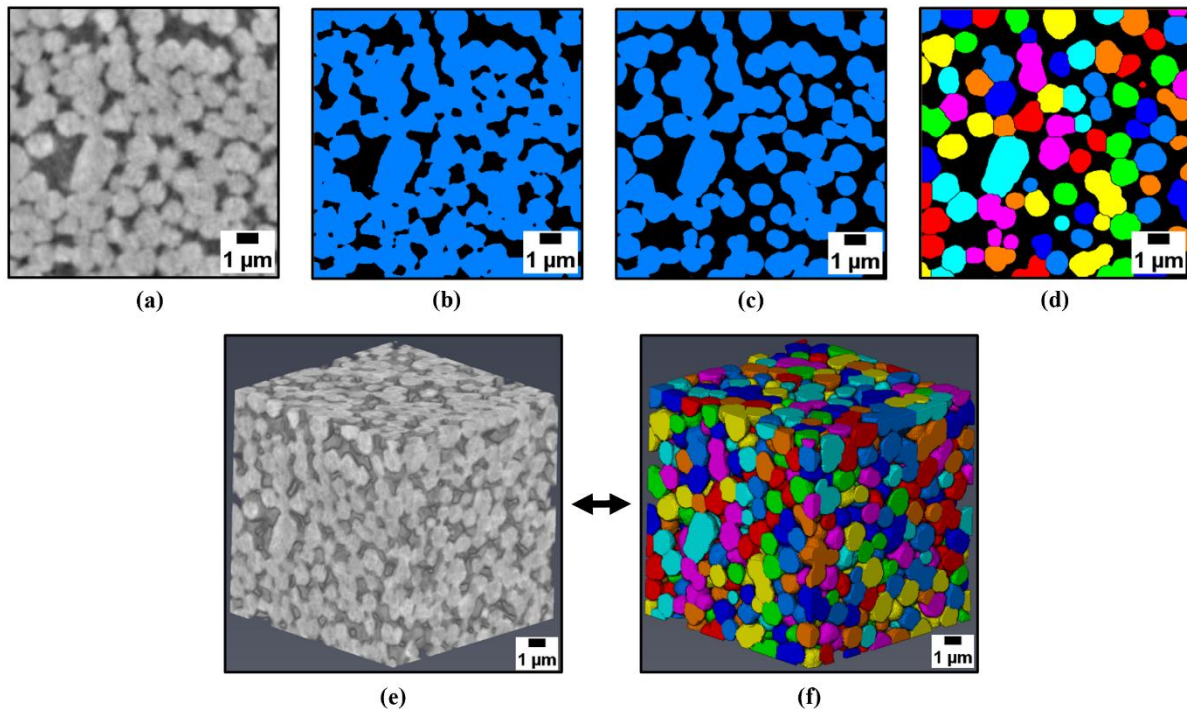


**Figure 4.** Steps of image improvement leading to segmentation, showing different pre-processing operations for a (a) raw image data - (b) binarization, (c) morphological opening and (d) watershed segmentation followed by labelling of grains. 3D rendering of the initial volume and (f) its final segmented state.

*Interactive thresholding* - to convert the normalized image from before into a binarized image. While letting the threshold be chosen interactively, the image was split up into two classes - voxels of interest, i.e., the grains here in blue and the background, i.e., the pores in black (**Figure 4** (b)). A grayscale normalization was performed prior to thresholding to facilitate consistency and enhancement of the contrast in the image.

*Opening* - operation carried out next to smoothen the inconsistencies along the edges of the grains observed in **Figure 4** (b). It is a combination of morphological operations in 3D - erosion, which shrinks the object, followed by dilation, using a structuring element. This ends up smoothening the contours of the grains while eliminating isolated pixels (**Figure 4** (c)). A

precise mode is chosen in Avizo, which ensures a structuring element matching a real sphere, referred to as ball opening, with half-kernel sizes (value of 2).

*Segmentation and labelling* - to split the connected components from the thresholded image for further analyses by means of separate objects module. This module performs a marker-based watershed segmentation on a distance map. The image is processed as a whole in 3D, adjusting the values of the markers (value of 2). More on watershed in the context of image processing could be found in the review work of Kornilov *et al.* [36]. The process largely fares well overall, assigning different colors to the segmented components, except in some cases where it fails to separate a few of the merged grains (**Figure 4** (d)). On rendering in 3D, the segmentation outcome looks like **Figure 4** (f) when compared to its original version in **Figure 4** (e).

Further, a label analysis module was used on the separated objects to extract a variety of statistical and numerical quantitative measures in 3D.

### 1.3 Results and discussion

During the in-situ measurements, the heat treatment for the two alumina samples in the furnace consisted of an increment with a rapid rate of around 40°C/min till 1500°C, and then an isothermal stay, with breaks at pre-meditated time-steps for the 4-distance imaging. For alumina with 1.3 µm particle size - Al 1.3µm, the imaging was carried out after 20 min, 40 min, 1 hour, 1.5, 2, 3 and 5 hours at 1500°C; while for Al 0.7µm, the time-steps were set at 10 min, 20 min, 30 min, 45 min, 1 hour and 2 hours of isothermal sintering. The reconstructed volumes were then treated to the image processing workflow proposed in **section 1.2.4**.

Unfortunately, for both the samples, it was not possible to follow the same regions for the initial two time-steps, even with the alignment technique in the SPAM software [33]. Pronounced particle rearrangement phenomena was noticed, as the image sections had different sets of particles with a considerable change in their numbers. The phenomena seemed to stabilize soon after and the same image sections could then be tracked in SPAM.

Particle rearrangement is an aspect of sintering which has not been thoroughly studied yet. There are, however, experimental evidence of its existence and its influence on the densification process in the initial stages of solid state sintering in the studies, to cite a few, by Exner *et al.* [37], Nöthe *et al.* [7], Wonish *et al.* [38], Wang *et al.* [39], McDonald *et al.* [40]

etc. The classical theories, however, do not account for particle rearrangement, and rather only hold diffusion related mechanisms to be responsible for densification.

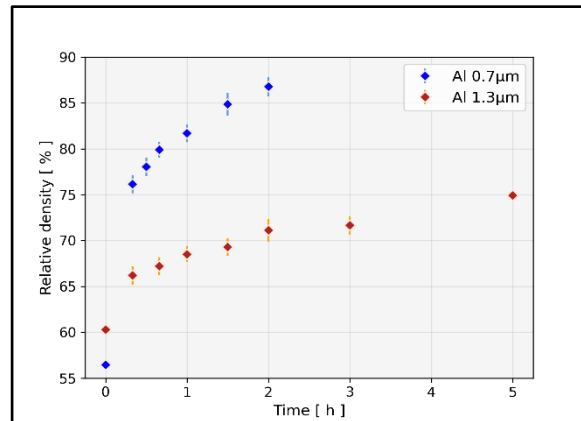


**Figure 5. Relative densities as a function of time for the sintered samples of Al 0.7µm and Al 1.3µm.**

The densities attained at the time-steps were determined using the ImageJ software [41]. Their progression with time is plotted in **Figure 5**. After 5 hours at 1500°C, the relative densities moved from ~60% to ~75% in the case of Al 1.3µm. For Al 0.7µm, the density rose to ~87% after 2 hours of sintering. A sharp rise in density was observed for the first time-step, with a gradual increment later on. Based on the densities reached, the samples ought to be in the initial (till ~70% of density) and intermediate (~70 to ~90% of density) stages of sintering. The time constraints with respect to the in-situ set-up were not conducive enough to let the samples reach the final stage (over 90% of density).

For the time-steps that were possible to be followed-up, evolution in one of the cross-section slices of the 3D reconstructed alumina samples of 1.3 µm and 0.7 µm are displayed in **Figure 6**.

The grain segmentation methodology proved feasible for Al 1.3µm but not for Al 0.7µm. Consequently, quantitative analyses that require an effective segmentation such as the evolution of the inter-particle necks and grain shapes have been achieved with Al 1.3µm only. And, the analyses that do not need a segmentation, like the progression of the grain and the pore sizes, and the pore curvatures, were carried out for both the powders.

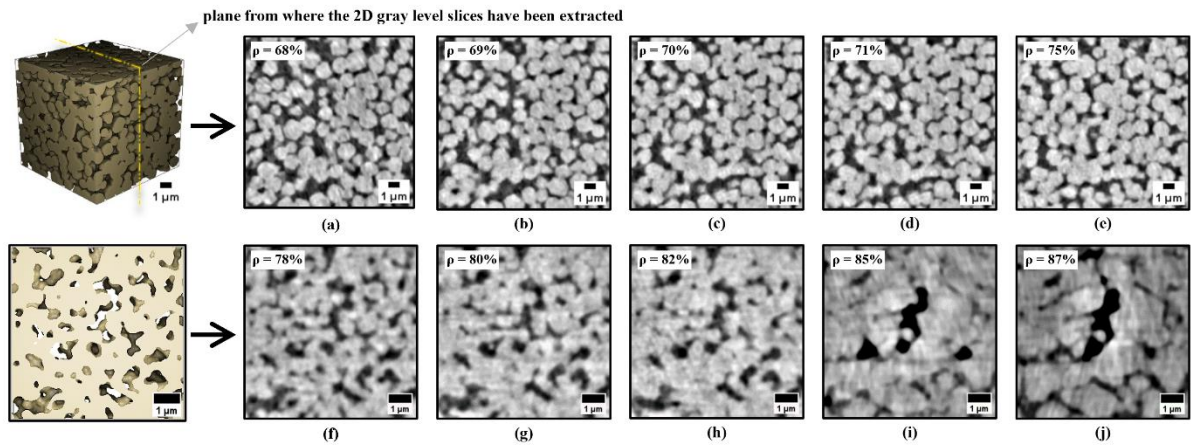


**Figure 6.** Follow-up of a cropped section (isometric 3D rendering) of the in-situ observation of the 3D reconstructed Al 1.3 $\mu\text{m}$ , after (a) 1 hour, (b) 1.5 hours (c) 2 hours, (d) 3 hours, and (e) 5 hours of sintering at 1500 $^{\circ}\text{C}$  respectively, and follow-up of a cropped section (side view of the 3D rendering) of the in-situ observation of the 3D reconstructed Al 0.7 $\mu\text{m}$ , after (f) 20 min, (g) 30 min (h) 45 min, (i) 1 hour, and (j) 2 hours of sintering at 1500 $^{\circ}\text{C}$  respectively. The relative density values ‘ $\rho$ ’ are mentioned on top-left. Scale bar is 1  $\mu\text{m}$ .

### *Grain size and pore size estimation*

The size of the evolving grains was estimated using granulometric analysis in the GeoDict image processing software. A thorough explanation of the algorithm and its implementation is contained in [42]. Granulometry does not require the separation of individual particles as it is only a geometrical assessment. Another method to estimate grain size involves segmenting the grains into separate entities. As detailed in **section 1.2.4**, after the segmentation in Avizo, label analysis was carried out on the grains to measure their sizes to later average them by volume. Meanwhile, the pore phase was subjected to only granulometry analysis in GeoDict as the separation of individual pores would be a rather vague exercise [43].

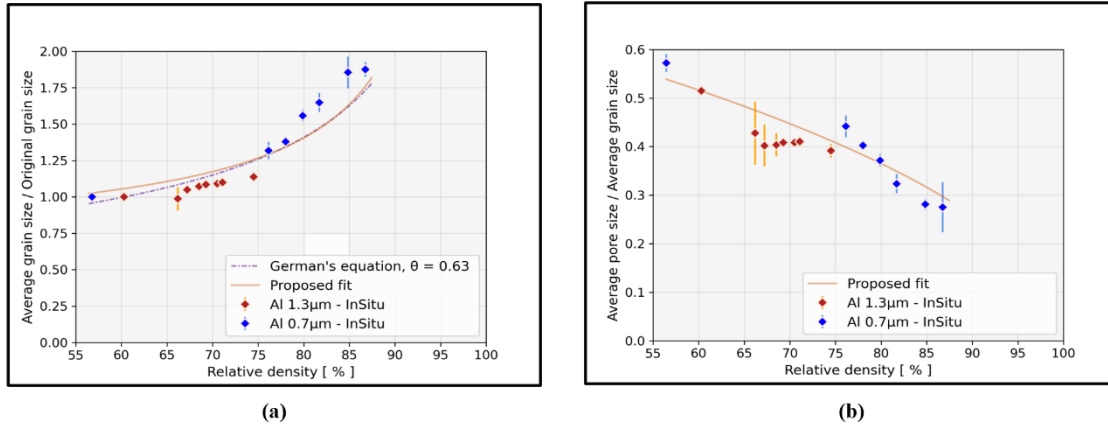


**Figure 7. (a) Comparison of average grain size over original grain size versus density for the two alumina samples, Al 0.7µm and Al 1.3µm, along with the corresponding curve-fit according to the equations proposed by German [44] and Venkatesh et al. [22]. (b) Comparison of average pore size over original grain size versus density for the two alumina samples, Al 0.7µm and Al 1.3µm, along with the corresponding curve-fit according to the equations proposed in Venkatesh et al. [22].**

### *Grain size evolution*

For the in-situ image stacks here for both the alumina powders, grain size measurements by means of granulometry were taken from multiple cropped stacks at different regions in the image over each time-step. The evolution of grain size was noted and plotted on a graph of average grain size over original grain size versus the relative density attained at those time-steps (**Figure 7 (a)**). The variability of data at each time-step was taken into consideration and plotted in terms of error bars.

For Al 1.3µm, the variability, mostly limited in its range, suggests that the grain growth is homogeneous at this stage of the sintering. The relatively higher variability at the first time-step could be a consequence of the observed particle rearrangement phenomena. The grain size progression is almost flat and shows no considerable increase till the density of ~75% is reached. The 2D stack follow-up shown earlier in **Figure 6 (a) (b) (c) (d) (e)** substantiates this size progression behavior. Additionally, post segmentation, grains were also measured individually in the case of Al 1.3µm. This method gave out similar outcomes as in the granulometric analysis, as the density is limited to ~75%. However, beyond this density, at later stages of sintering, a convergence in the values cannot be expected due to failure of the segmentation approach.

For Al 0.7 $\mu\text{m}$  though, a significant increase is seen at each passing time-step, together with slight changes in the variability of the data. The average grain size gets almost doubled on reaching a density of  $\sim 87\%$ . The fact that the smaller alumina powder Al 0.7 $\mu\text{m}$  shows a relatively faster densification coupled with a more intense grain growth is reflected in the **Figure 6** (f) (g) (h) (i) (j), displayed earlier. Rapid disappearance of grains, mostly the smaller ones, could be noticed over time as well, acting as a reason for increasing the average grain size.

To track the grain size progression, in Venkatesh *et al.* [22], an equation proposed by German [44], [45],  $G = \frac{G_o \theta}{\sqrt{1-f}}$ , was found to deviate from the obtained points at densities over 85%. In this equation,  $G_o$  is the initial grain size,  $\theta$  is a constant with a value of 0.6, and  $f$  is the grain volume fraction. A revised equation covering all the points in a reasonable manner was hence proposed, which read  $\frac{G}{G_o} = a \exp\left(\frac{b}{\sqrt{1-f}}\right)$ , with two constants,  $a = \sim 0.5$  and  $b = \sim 0.4$  respectively. As the maximum densities do not go well past 85%, both the above stated equations fare well here by coming close to encompass the obtained range for the grain size values for both the powders, as seen in **Figure 7** (a).

Furthermore, although from **Figure 6** (a) (b) (c) (d) (e) and **Figure 7** (a), it could be assumed that the whole of Al 1.3 $\mu\text{m}$  would report a regular grain growth behavior at this stage of sintering, taking advantage of the available in-situ images, a closer local observation was attempted. Interestingly enough, it revealed localized heterogeneities at a few locations. **Figure 8** shows one such instance.

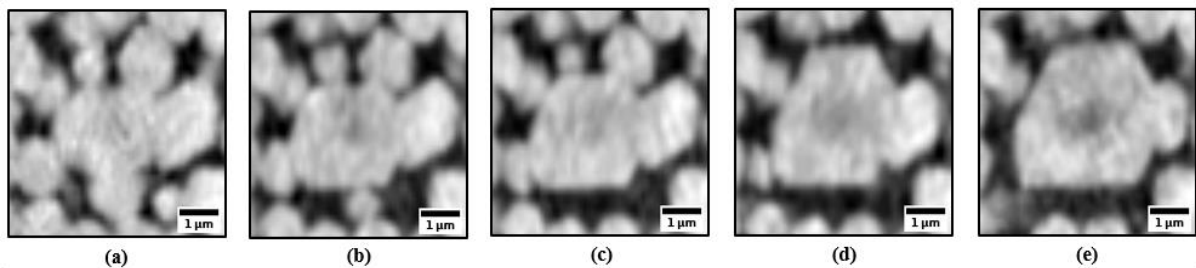


**Figure 8.** Follow-up of the particle coarsening phenomena for the in-situ observation of Al 1.3 $\mu\text{m}$  after (a) 1 hour, (a) 1.5 hours (c) 2 hours, (d) 3 hours, and (e) 5 hours of sintering at 1500 $^{\circ}\text{C}$  respectively.

This set of images displays a disproportionate consumption of the smaller grains, leading to their gradual disappearance over time. This feature of coalescence, where two grains merge to

create a single grain progressively, is a prominent aspect of grain growth and is generally a highlight of the final stage of sintering.

Nevertheless, Kang [4] and Rahaman [3], in their review publications on sintering, have cited peculiar situations which could lead to such particle coarsening in the initial stages. According to German [44], this type of behavior could arise in the case of large grain size differences - the larger grains would eventually eat their smaller neighbors and grow at their expense. As the larger grains have a lower surface energy per unit volume, incremental surface diffusion events across the neck interface progressively swell them up while eroding away the smaller neighboring grains with a higher surface energy. Coarsening becomes much more prominent in the late intermediate and the final stages of sintering, but unfortunately the images available here are limited to a relative density of 76%. Further pursuit beyond this density would bring an added value to check the preferential growth of these large grains developing from the initial large seed particles and their influence over time on the overall microstructural evolution.

Yet, this local phenomenon does not have a significant impact on the overall behavior and statistics, as evident from the negligible variability in the data from the graph.

### ***Pore size evolution***

Together with the grain size estimation, a clearer interpretation of microstructural development also requires an understanding of how the pore network develops. An estimation of the pore size evolution, normalized with respect to the average grain size, is therefore plotted as a function of density in **Figure 7 (b)**.

In the case of Al 1.3 $\mu\text{m}$ , a limited reduction in the pore size can be seen. The size ratio decreases from the initial  $\sim 0.5$  to  $\sim 0.4$  after 75% density. As observed in **Figure 6 (a) (b) (c) (d) (e)**, the pore phase is still continuous, since the sintering is still in the intermediate stage. On the contrary, as Al 0.7 $\mu\text{m}$  has been sintered till around 90%, gradual changes in the pore network, initially all connected, could be observed in **Figure 6 (f) (g) (h) (i) (j)**. The larger pores originally present in the initial green state shrink, coinciding with an increase in the densification. As a result, a much sharper reduction in the average pore size is noticed in **Figure 7 (b)**, as compared to the evolution in Al 1.3 $\mu\text{m}$ . The pore size has nearly halved from  $\sim 0.6$  to begin with to  $\sim 0.3$  on reaching  $\sim 87\%$  density.

Moreover, a larger variability in the data could be noted here in the pore size evolution as opposed to the grain size observations. This could be due to the fact that the porosity could be larger in areas where the initial packing was not optimal.

As in the case of grain size evolution, an equation valid for all the stages of sintering,  $p = G \left( \frac{\varepsilon}{1.5} \right)^{1/2}$ , where  $p$  is the average pore size,  $\varepsilon$  is the pore volume fraction and  $G$  is the average grain size, was proposed in Venkatesh *et al.* [22] to predict the evolution of the pore size. The proposed equation fits well and passes through the range of pore size values at each time-step for the in-situ images.

To corroborate the above-mentioned findings, a local observation was also carried out on the porosity phase of Al 0.7 $\mu\text{m}$ , the 3D renderings of which are displayed in **Figure 9**. It captures the interplay of a variety of phenomena in the pore network, such as the large pore in the center (in yellow) getting ruptured and steadily losing its branches; the pores smaller in size (in pink) disappearing completely; and some of the bigger pores either remaining the same or slightly growing (in white).

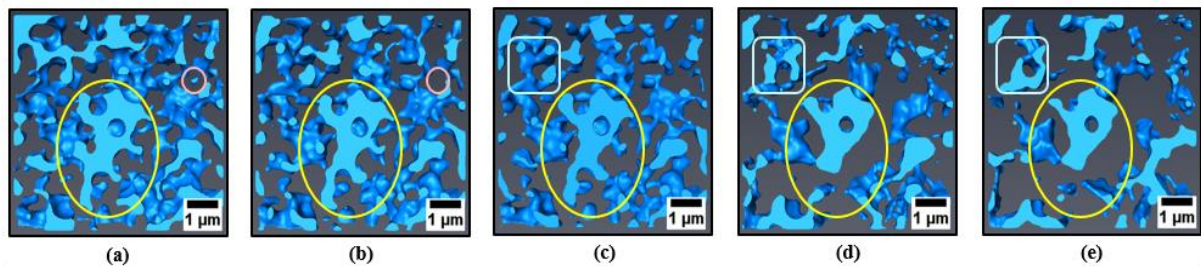


**Figure 9.** Follow-up of the mechanisms occurring in the pore network for the in-situ observation of Al 0.7 $\mu\text{m}$  after (a) 20 min, (b) 30 min, (c) 45 min, (d) 1 hour and (e) 2 hours of sintering at 1500°C respectively.

### *Grain shape evolution*

For obvious reasons, grain shape variations during ceramic sintering have never really been tracked and observed at the particle scale. Here, morphological changes in the grain shapes have been investigated through the evolution in values of their sphericity and smoothness. For this purpose, image stacks after Avizo-segmentation (**section 1.2.4**) were fed into the GrainFind module of GeoDict [42]. The discussion here is limited to Al 1.3 $\mu\text{m}$  as the observations on Al 0.7 $\mu\text{m}$  and consequently their grain segmentation are relatively harder.

The sphericity analysis in the module allows for the best possible grain-fit in terms of ellipsoids into each segmented grain. While there are a lot of ways in which sphericity could be defined and calculated, Krumbein's definition of sphericity [46], which is an isotropic measure, reading,  $S = \sqrt[3]{\frac{bc}{a^3}}$  is adopted in this work. a, b, and c are the three principal axes of the ellipsoid (with 'a' being the length of the longest axis, while 'b' and 'c' are the lengths of the other two shorter axes). S takes the values from 0 to 1, with 1 marking a perfectly isotropic grain.

For the in-situ image stacks of Al 1.3 $\mu\text{m}$ , as in **Figure 10**, the Krumbein sphericity values obtained are plotted against their relative frequency.

At the green state, we expected our almost-rounded Al 1.3 $\mu\text{m}$  powder to have a sphericity of close to 1. However, as seen in **Figure 10** (a), the sphericity in the initial state is spread across a range of values. This goes on to say that the powder system indeed consists of particles that are anisotropic in nature. After 20 min of sintering, at the first time-step (**Figure 10** (b)), a sharp transition in the values is seen in the graph. The sphericity values then shift gradually to the right from **Figure 10** (b) onwards at every time-step till ~1 hour of sintering (**Figure 10** (c)). Later, a slight indication of a leftward shift is observed for the images after 5 hours, as in **Figure 10** (e). After this point, with prolonged heating and the resulting progressive increase in grain size, the sphericity values are speculated to decrease and further move to the left. The underlying reason for this behavior is pursued with the help of scatter plots, displayed adjacent to the corresponding sphericity assessments. The plots classify the shape of the fitted ellipsoids into 4 categories: spheres, prolates, oblates and flat-bars. Spheres have equal lengths for all three axes of the ellipsoid. Prolates have one axis longer than the other two, which are equal. Oblates have one axis shorter than the other two, which are equal. And, flat-bars have two axes much shorter than the third one.

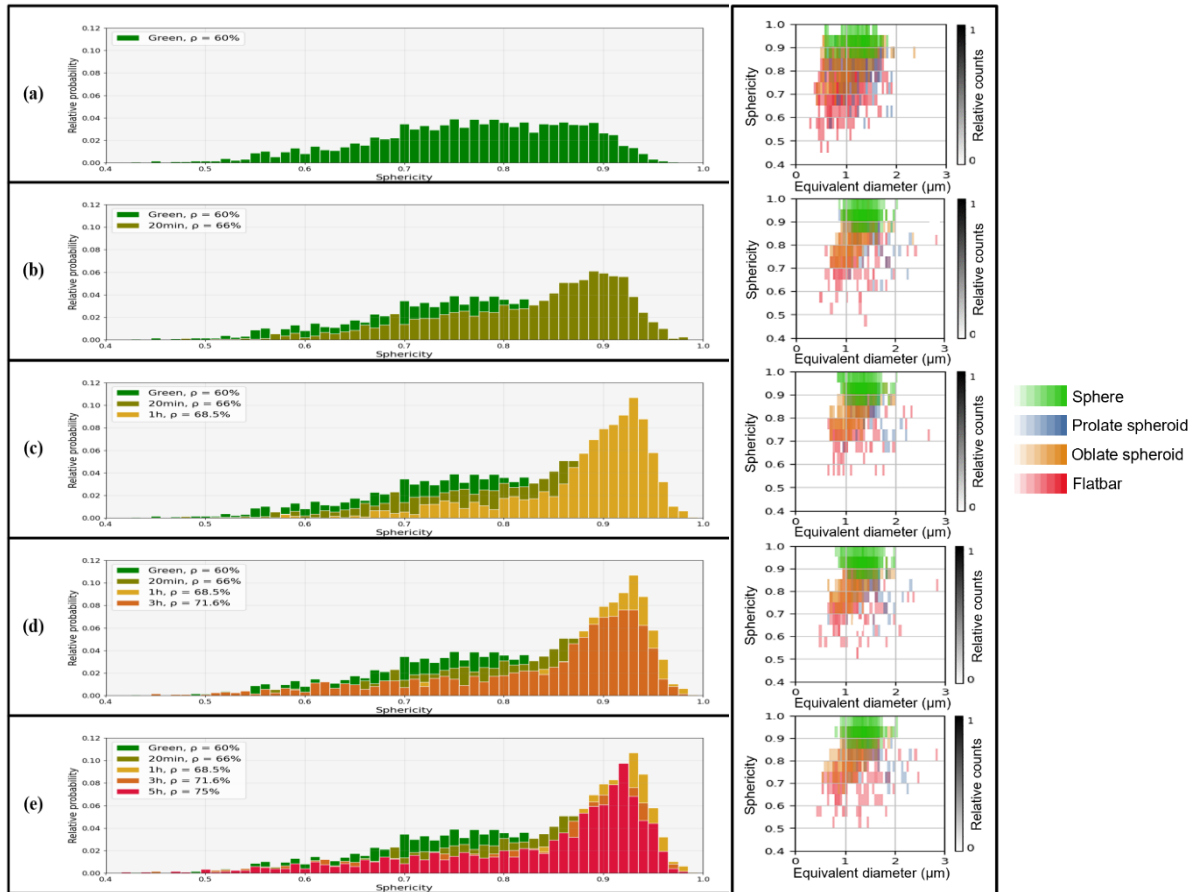


**Figure 10. Evolution of sphericity for the in-situ X-ray nano-CT observation of Al 1.3 $\mu\text{m}$  at (a) the green state, and after (b) 20 mins, (c) 1 hour, (d) 3 hours and (d) 5 hours of sintering at 1500 $^{\circ}\text{C}$  respectively, with their corresponding scatter plots.**

Equivalent diameter and the sphericity of the particles, together with their relative counts, are chosen as the variables for the plot. Comparing the first two plots, it is evident that a large number of non-spherical particles tend to disappear or turn close to spherical at the very first time-step. Also, to be noted is that these are mainly the smallest particles in the considered stack. The grains could have also simply merged with their neighbors as a consequence of particle coarsening detailed earlier. The subsequent plots show a similar trend, with less drastic changes. However, the number of spherical particles either increases slightly or remains stable throughout the time-steps in consideration. The relatively larger particles appear to stay put. Towards the end, after 5 hours, a marginal increase in the number of irregular particles could be observed, which is probably because of grain interactions leading to improper segmentation.

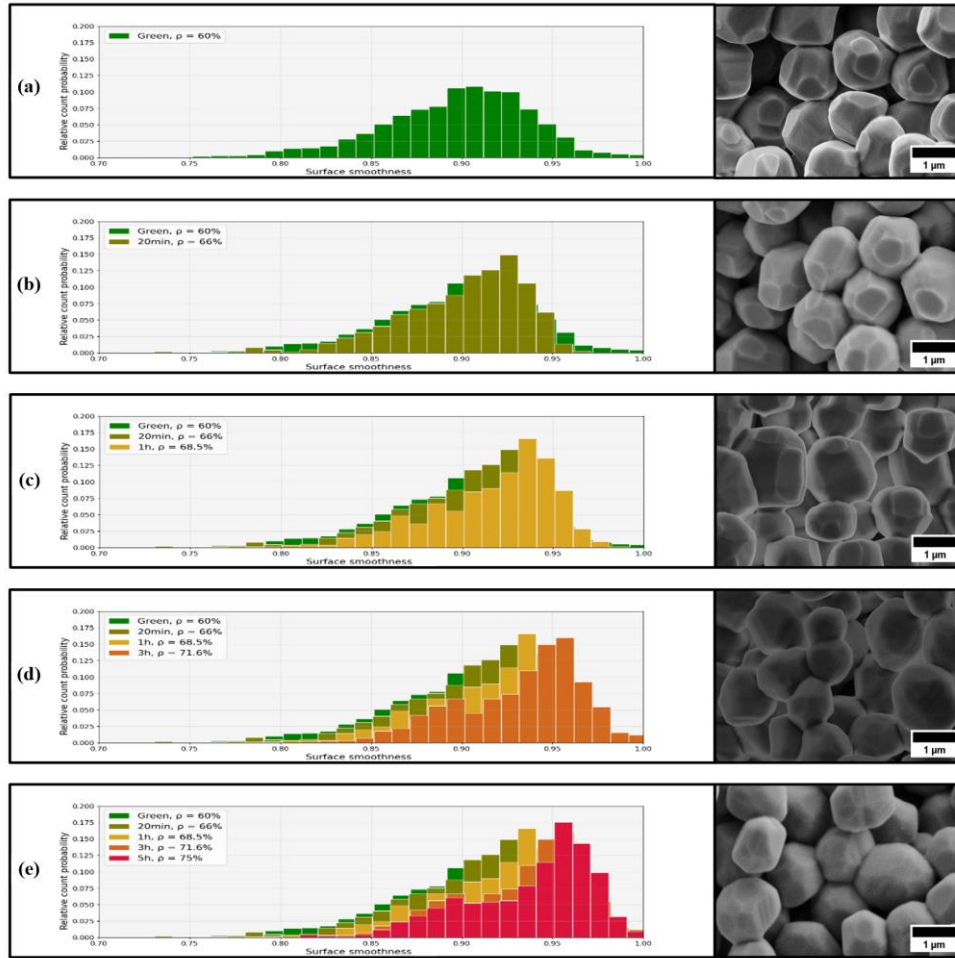


**Figure 11.** Evolution of surface smoothness for the in-situ X-ray nano-CT observation of Al 1.3µm at (a) the green state, and after (b) 20 mins, (c) 1 hour, (d) 3 hours and (e) 5 hours of sintering at 1500°C respectively, with their corresponding SEM observations.

Another aspect that we investigated with regard to the grain shape was the variations in the smoothness of the surface of the grains over time. We used a method that calculates the surface of the segmented grains by an algorithm put forth by Ohser *et al.* [47]. The smoothness value of each grain is then based on the surface of the best-possible-ellipsoid-fit into these grains divided by the algorithm-calculated surface. The values range from 0 to 1, where 1 means the grain is perfectly rounded.

**Figure 11** shows the probability plot for the surface smoothness. Although the average value of the smoothness value is around 0.9 initially, the distribution hints at the presence of grains having rougher surfaces than others. Further, as time progresses, we observe that the smoothness value only increases, indicating the consequent smoothing of the grains. Surface diffusion is expected to be behind this transition, as the diffusion mechanism would first smoothen the edges and corners of the polyhedral shape and transform it into a smoother version of the same. Combining this assessment with the earlier observation in the sphericity

section, smaller grains which seem to vanish at the start could have been aided by their relatively faster tendency to undergo diffusion mechanisms. This would result in a better fit of the ellipsoid approximation, ensuing in an increase in the smoothness values.

To cross-check the observed phenomena, since we could not co-relate the first few of the tomography images (**section 1.3**), samples sintered up to the given time-steps were subjected to SEM examinations. The observations, shown besides each time-step for the in-situ graphs in **Figure 11**, were carried out using secondary electrons, SE2, so as to capture the details from an angle, with good topological contrast. The SEM studies reveal that the presence of facets in the initial polyhedral is responsible for the lower smoothness values. The initial particles are seen to turn smoother before the actual sintering begins; and over time, the facets can clearly be observed to disappear. This confirms the initial increase noticed in the smoothness plots and their stabilization later. Also, with increasing time, grains appear to come closer towards each other as a consequence of sintering.

Integrating the observations from the plots presented in the section, one or more factors that influence the grain shape behavior can be summarized as follows:

- Smaller irregular grains tend to merge with other grains due to the particle coarsening phenomenon discussed in the previous section.
- Smaller grains also experience a faster diffusion process than larger grains, resulting from shorter diffusion paths. This is supplemented by the loss of facets and the formation of smoother and isotropic grains.
- Larger or regular grains mostly maintain their shape and size in the initial stages of sintering.

The grain shape phenomenon observed in such particular powder systems, coupled with thorough research on the geometrical aspects involved could evidently bring about valuable new information to the modelling realm. The classical theories of sintering are generally described using idealized models represented by spheres for the initial stage; while the grains are assumed to adopt the shape of a tetrakaidecahedron, enclosing cylindrical-shaped pore channels at their edges in the intermediate stage; and spherical pores at their corners for the final stage [3], [4]. A fully accurate module as per Coble *et al.* [48] should take into account progressive changes in grain shapes. And, according to German, a comprehensive analysis on grain shape progression could lead to the usage of grain shape, instead of grain size, as the basis for predicting grain growth or shrinkage [44].

## Neck growth

The commencement of sintering is marked by the formation of so-called necks at the particle junctions. These necks show an incremental evolution during sintering and their quantification serves as an ideal indicator to monitor the progress of sintering. The high-resolution 3D images here permit us to visualize the necks at the local level and are therefore well-suited to provide a better picture.

As the grain segmentation with regard to Al  $0.7\mu\text{m}$  does not yield satisfactory results because of higher densities, the analyses were carried out only on Al  $1.3\mu\text{m}$ . (see section 2 of *Supplementary Information* for details on the steps involved in the retrieval of necks).

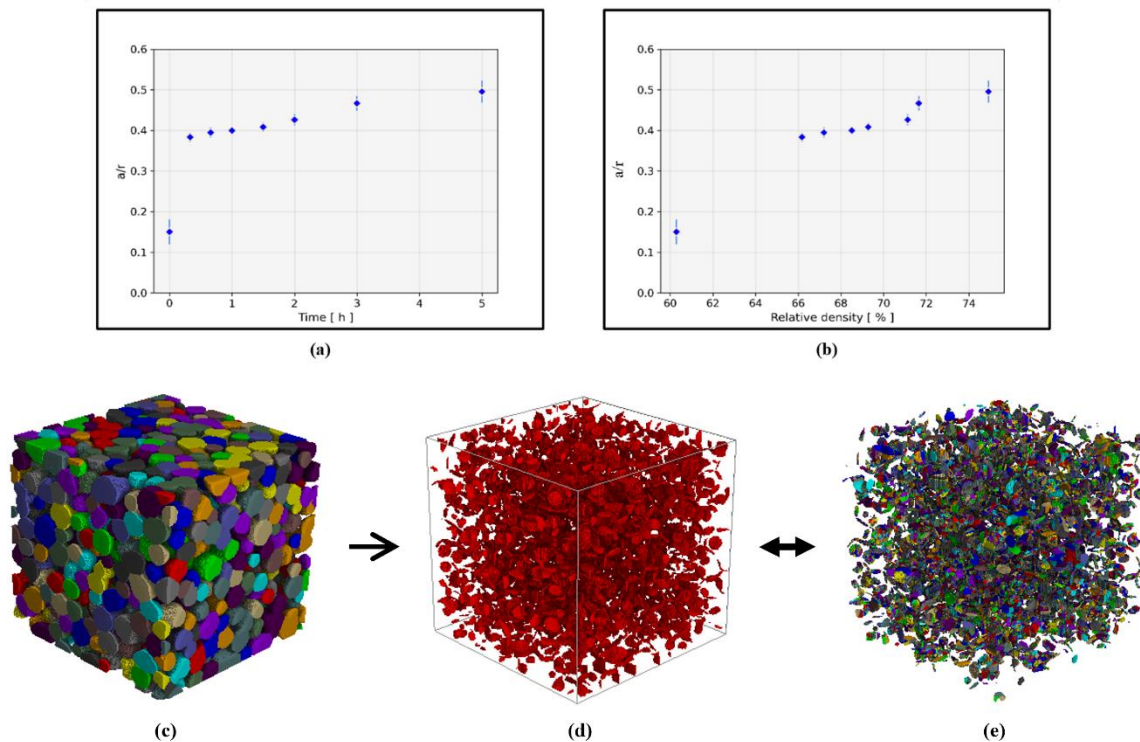


**Figure 12. (a) Growth of the average inter-particle neck ratio (a) over time and (b) versus density for the alumina Al  $1.3\mu\text{m}$ . Close-up of (c) cropped segmented section of alumina Al  $1.3\mu\text{m}$  and its corresponding neck morphology, (d) prior to segmentation and (e) post-segmentation.**

Neck growth is commonly expressed as the change in neck size ratio, a dimensionless parameter corresponding to the ratio of the neck radius 'a' to the particle radius 'r' (half of the average grain size). This ratio denotes the degree of sintering and, as per German [45], the value of the ratio up until 0.5 corresponds to initial and intermediate stages of sintering, and

more than 0.5 to the final stage of sintering. This makes 0.5 the transitional value between intermediate and final stages.

**Figure 12** (a) shows a plot of the average neck size ratio versus the sintering time taken from different VOIs for Al 1.3 $\mu\text{m}$ , with the corresponding variability in the data. The neck size ratio, taken into account from the time  $t = 0$  of the sintering plateau already has a value of  $\sim 0.15$ . A huge increment in the value can be observed for the first time-step of 20 min. Later, with increasing time, the average neck ratio ‘a/r’ shows a progressive increase. From a density perspective (**Figure 12** (b)), the values go from  $\sim 0.15$  to  $\sim 0.5$  for the densities from  $\sim 60\%$  to  $\sim 76\%$  after 5 hours. The ratio would further certainly increase beyond 0.5 with an increase in sinter time, while not having yet reached the final stage of sintering. The trajectory would therefore go on and not satisfy the postulation by German mentioned above.

With regard to neck growth kinetics, many models are found in publications by Kuczynski *et al.* [49], Kingery *et al.* [50], Coble *et al.* [51] and Johnson *et al.* [52]. They have been summarized and expressed in a general form by Rahaman [3] as  $\left(\frac{a}{r}\right)^m = \frac{H}{r^n} t$ , where ‘H’ is a term made up of material and geometrical parameters of the powder system, while ‘m’ and ‘n’ are constants typically with values corresponding to a sintering mechanism. The retrieval of ‘m’ from this time-dependent neck growth behavior would then hint at the possible sintering mechanism and thereby the different growth kinetics acting on the system at different times.

However, the linear fitting in this case has been unsuccessful, pointing out the fact that the powder system in hand is too far away from an ideal system assumed in the model. The model fares well for two spheres equal in size, but as seen in **Figure 12** (c) (d) (e), Al 1.3 $\mu\text{m}$  constitutes particles of different sizes and shapes and, consequently, necks of different sizes and shapes. Furthermore, the expression above assumes a point contact at the beginning of the sintering plateau, which is not the case in this context as well.

### Curvature maps

Two shape indicators, namely, Shape Index (S) and Curvedness (C) were found to be well-poised to quantify the 3D morphology of pore-solid interface curvature. These two indicators are formulated as,  $S = \frac{2}{\pi} \arctan\left(\frac{k_1+k_2}{k_1-k_2}\right)$  and  $C = \sqrt{\frac{k_1^2+k_2^2}{2}}$ , respectively.  $k_1$  and  $k_2$  in the equations are the principal curvatures. These representations are de-coupled from one another and represent distinct properties of a surface [53], [54]. The shape index conveys relevant information on the shapes surrounding surface points, while curvedness is a measure of deviation from a flat surface [55]. These indicators can be computed and interpreted in terms of 2D histograms called ‘curvature maps’, normalized with a probability density P(S,C).

The constituents of the curvature map, shape index and curvedness are represented as in **Figure 13** for a visual comprehension.

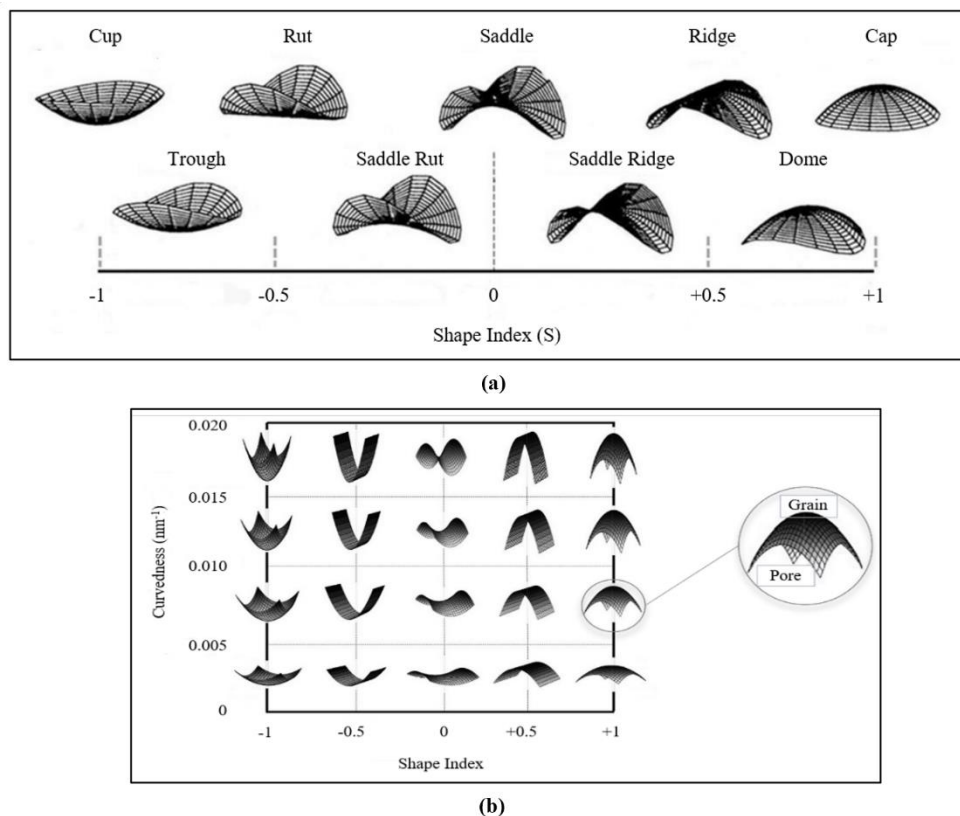


**Figure 13.** (a) Several local shapes fitted in the shape index profile [54], (b) depiction of increasing curvedness values with respect to shape index (adapted from Burr *et al.* [57]).

**Figure 13** (a) shows an array of local shapes with their corresponding shape indices. The shape index carries all the pertinent information in the form of a single number, either negative or positive, to wholly describe interfacial shapes, as opposed to the requirement of two different measures, like the Gaussian and mean curvatures [55]. A concave-shaped cup-like profile has a shape index value of -1, while it is +1 for a convex-shaped cap-like profile. The convexities are separated from the concavities by a symmetric saddle-like profile in the middle with an index value of 0. **Figure 13** (b) indicates that the curvedness is a positive value, and an increase in its value represents a more angular surface. A flat plane would have a value of 0 for both the shape index and the curvedness.

Preceding study on pore curvature maps in Venkatesh *et al.* [22] demonstrated their potential to trace the distribution of the pore-interface shapes for the set of post-mortem image stacks at different sintering time intervals. Taking a cue from this, with an aim of capturing the pore interface shape evolution in the initial stage of sintering, curvature maps in the (S,C) plane were plotted as in **Figure 14**, for the 3D renderings of the in-situ image stacks of Al 1.3 $\mu\text{m}$ . With reference to the shape index profile in **Figure 13** (a) (b), the initial spread after 1 hour of sintering primarily comprised of rut-like shapes (**Figure 14** (a)). The distribution then showed a clear, continuous movement in the rightward direction (**Figure 14** (b) (c)), with increasing sinter time and density. The shapes gradually evolved and concentrated around different saddle-like shapes on reaching  $\sim 75\%$  relative density after 5 hours of sintering in **Figure 14** (d). These cylindrical saddle shapes represent the interconnected open porosity present at this stage, formed as a consequence of neck growth and the resulting densification.

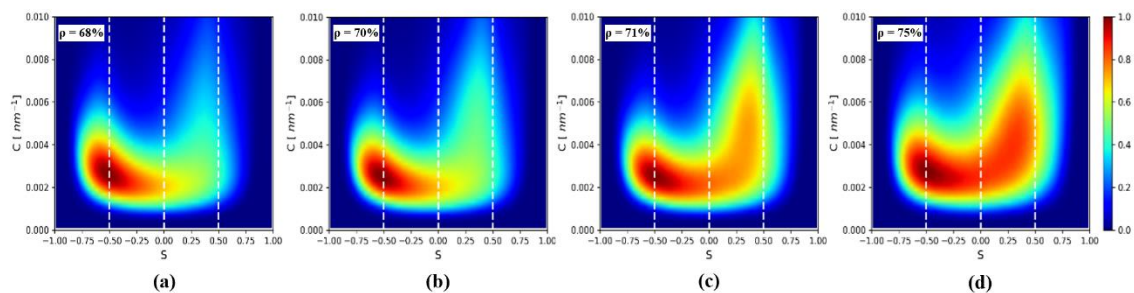


**Figure 14.** Pore curvature maps for the in-situ observation of Al 1.3 $\mu\text{m}$  after (a) 1 hour, (a) 2 hours, (c) 3 hours and (d) 5 hours of sintering at 1500 $^{\circ}\text{C}$  respectively.

Furthermore, as the available Al 1.3 $\mu\text{m}$  stacks are restricted to  $\sim 75\%$  density, in order to check the behavior of the maps at a higher density, Al 0.7 $\mu\text{m}$  image stacks were used as they already attain 76% of density after just 10 min of sintering. The curvature maps are plotted for Al 0.7 $\mu\text{m}$  in **Figure 15**. The probability density P in the maps is around the saddle-like shapes in **Figure 15** (a). With increasing density, in **Figure 15** (b) and (c), a transformation in the distribution is observed and P moves significantly to the right, going past the saddle shapes and settling around ridge-like shapes (shape index of  $\sim 0.5$ ).

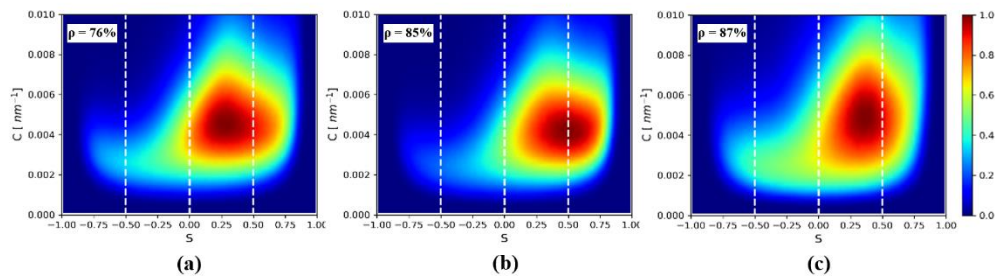


**Figure 15. Pore curvature maps for the in-situ observation of Al 0.7 $\mu\text{m}$  after (a) 10min, (b) 1 hour and (c) 2 hours of sintering at 1500°C respectively.**

Although they are two different powders, we can gather **Figure 14** and **Figure 15** in order to trace a continuum of sorts. With this information, it is safe to assume that the maps for Al 1.3 $\mu\text{m}$ , except for their shape, would have undergone a transition at just about 75% density and converged into a distribution like the one seen in **Figure 15** (a) onwards, only to further follow the rest of the map and keep moving to the right during the course of sintering.

This is consistent with the observations made for the post-mortem stacks in Venkatesh *et al.* [22]. The distribution there moved from the left and advanced towards the right with each passing time interval. Taking advantage of this, an attempt was made to categorize the sintering process into two distinct stages based on the evolution of the pore shapes: an initial stage with more of cup-like pores and another stage corresponding to cap-like pores. The maps there, however, missed out on the changeovers occurring in between particular time intervals. Although, here, the interrupted in-situ observations do not necessarily disclose startling new information, the time-steps of much shorter extent succeed in giving an added visual information to explain the phenomenon of gradual shifts in the maps and the transition at around 75% density, which were only a subject of speculation in Venkatesh *et al.* [22].

Additionally, the in-situ images are predominantly expected to not just provide statistical changes over sintering time, but offer insights on how this statistical information could be

understood in terms of local observations. As the same set of microstructural details can be monitored, a follow-up of the pore-interface evolution would help decipher the curvature maps more precisely.

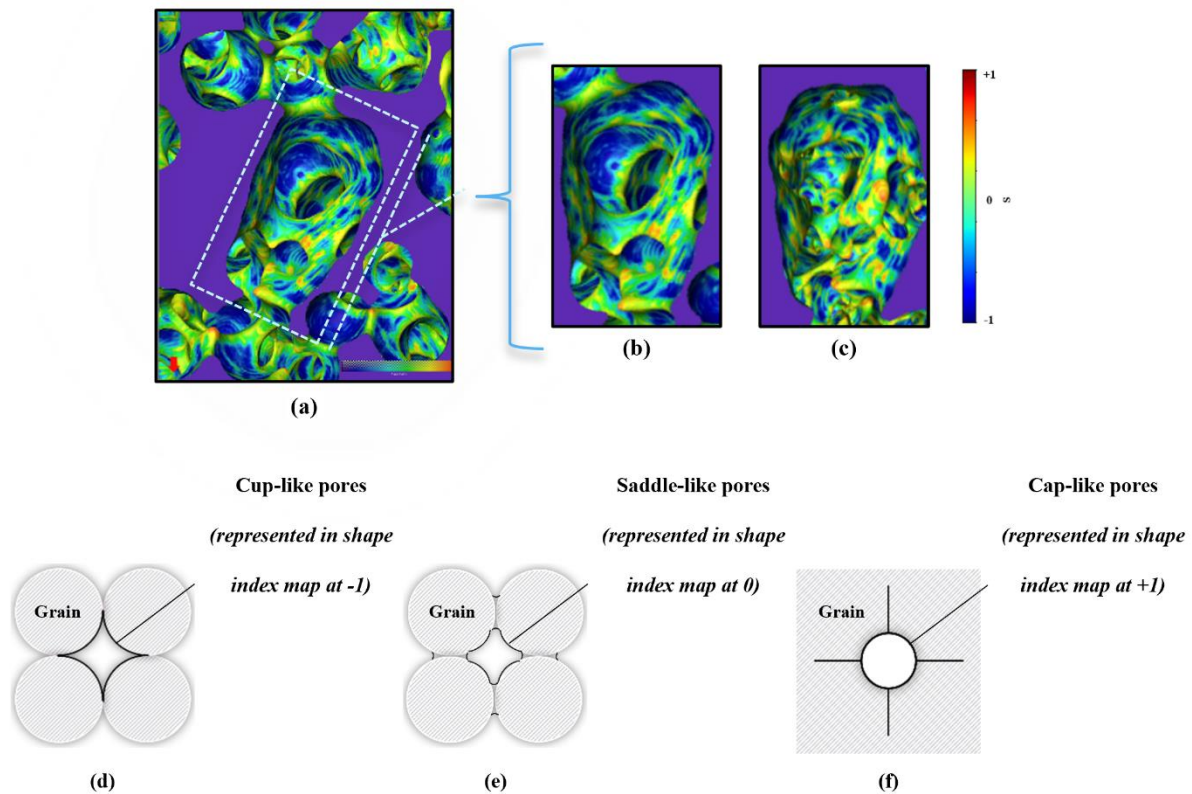


**Figure 16. Snapshots of the (a) 3D rendering of the shape index values of the evolving pore network, for the in-situ observation of Al 1.3 $\mu$ m after (b) 1 hour and (c) 5 hours of sintering at 1500°C respectively. Representation of pore evolution during the sintering process from (d) the initial cup-like pores to (f) the final cap-like pores, including an (e) intermediate transition step with saddle-like pores.**

Accordingly, a cropped section of the pore network is 3D rendered below in **Figure 16** (a) (b) (c). It shows the gradual local variation in the shape index values explained above. A closer look at the rendering from **Figure 16** (b) to **Figure 16** (c) shows an increasing number of higher intensity points on the scale bar for the shape index. This in turn suggests the gradual shape variation happening at the local surface level and the resulting rightward shift in the shape index profile.

Consequently, with this updated set of information obtained from the in-situ images, the novel way of classification of sintering proposed in Venkatesh *et al.* [22] based on pore shapes could be expanded from the previously defined 2 stages. A transition step could be integrated in between the cup-like shaped initial stage and the cap-like shaped final stage. This endorses the

classical understanding (**Figure 16** (d) (e) (f)) of sintering - the formation of closed porosity with an opposite curvature towards the end of sintering with regard to the pore curvature in the initial stage, together with an intermediate stage constituting a network of pore connectivity.

## 1.4 Conclusion

This paper showcases a first-of-its-kind in-situ nano-tomography experiment exploring the ceramic sintering process at high temperature and at the particle length-scale. The experiment was conducted using the phase contrast X-ray nano-holotomography technique at the European Synchrotron Radiation Facility (ESRF). A custom-made high temperature furnace, built for the purpose, proved fit enough to operate inside the synchrotron hutch for the entire duration of the experiments.

The value-addition brought about by in-situ techniques for investigating ceramic sintering is evident. By employing in-situ methods, the study was able to uncover not only the global alterations in the ceramic microstructure at various stages of sintering, but also, conveniently, the transient phenomena that occurred between the time-steps, by tracking the same particles over time.

We chose a model alumina powder system for the studies, and the high resolution of 25 nm attained allowed us to capture the collective behavior of the particles at different time intervals during the sintering process. Even though the powder system is rather simple compared to commonly used industrial powders, it is still complex and heterogenous as the local observations demonstrate.

Analysis on several key sintering parameters complemented by a thorough local assessment of the microstructure were attempted upon, using the 3D rendered data.

The parameter study included the progress of the size of the grains and the pores, and the inter-particle neck growth over time. Local examination revealed some uncommon phenomena, such as particle coarsening, at the early stages of sintering, which is usually a highlight of the latter stages of sintering. It was also possible to delve into critical unresolved aspects like particle shape evolution. Two indicators viz. sphericity and smoothness were used to describe the shape of the grains and their further advancements. Considering these shape effects and/or incorporating realistic grain shape behavior obtained by in-situ images should greatly enhance the quality of the simulation models. Underlying factors for each of these behaviors are reflected upon at the end of the respective sections.

Furthermore, the prospects of monitoring of the pore-interface curvature at different time-steps were exploited to classify the stages of sintering based on the shapes of the curvatures attained - two clearly distant stages corresponding to the pore shapes, with a transient step in between.

Expanding the scope of this research, a continuous in-situ examination at an even higher resolution could bring in more revelations. Concentration could be wholly directed, say, on the neck contact area to observe and track the mass transport phenomena. This could improve our understanding on the various diffusion mechanisms and could be incorporated into the existing models by integrating realistic parameters. A detailed study on the evolution of the shape of the necks should be possible as well.

Also, incorporating the latter stages of sintering, especially beyond 90% density, could provide 3D insights on a number of phenomena, such as the interaction between pores and grain boundaries that move as a result of grain growth, 3D visualization of pore closure transition, pore shrinkage during grain growth or the inability to do so, attachments of the pores to the grain boundary or their separation, pore annihilation, distortion in the pore shapes over time etc.

Nonetheless, this experiment is a significant step forward in understanding the underlying phenomena of ceramic sintering and can serve as a framework for future studies in this research area. Efforts are now being made to serve the obtained in-situ data as an input to one of the improved DEM models developed by the research group [56].

### **Acknowledgements**

This project has received funding from the European Union's Horizon 2020 research and innovation programme under the Marie Skłodowska-Curie grant agreement MATHEGRAM No 813202. The authors also thank the ESRF for the provision of synchrotron radiation facilities (Proposal MA4632).

## References

- [1] S. Somiya and Y. Moriyoshi, “Sintering Key Papers,” *Springer Science & Business Media*, 1990, doi: 10.1007/978-94-009-0741-6
- [2] R. M. German, “Sintering Theory and Practice,” *John Wiley & Sons, Inc.* 1996.
- [3] M. N. Rahaman, “Ceramic processing and sintering,” *CRC press*, 2003.
- [4] S.-J. L. Kang, “Sintering: densification, grain growth and microstructure,” *Elsevier*, 2005.
- [5] R. K. Bordia and E. A. Olevsky, “Advances in Sintering Science and Technology: Ceramic Transactions,” *John Wiley & Sons, Inc.*, 2009.
- [6] O. Lame, D. Bellet, M. Di Michiel, and D. Bouvard, “Bulk observation of metal powder sintering by X-ray synchrotron microtomography,” *Acta Materialia*, vol. 52, no. 4, pp. 977–984, Feb. 2004, doi: 10.1016/j.actamat.2003.10.032.
- [7] M. Nöthe, M. Schulze, R. Grupp, B. Kieback, and A. Haibel, “Investigation of Sintering of Spherical Copper Powder by Micro Focus Computed Tomography ( $\mu$ CT) and Synchrotron Tomography,” *Materials Science Forum*, vol. 539–543, pp. 2657–2662, Mar. 2007, doi: 10.4028/www.scientific.net/msf.539-543.2657.
- [8] L. Olmos, T. Takahashi, D. Bouvard, C. L. Martin, L. Salvo, D. Bellet, and M. Di Michiel, “Analysing the sintering of heterogeneous powder structures by in situ microtomography,” *Philosophical Magazine*, vol. 89, no. 32, pp. 2949–2965, Nov. 2009, doi: 10.1080/14786430903150225.
- [9] B. Kieback, M. Nöthe, J. Banhart, and R. Grupp, “Investigation of sintering processes by tomography,” *Materials Science Forum*, Trans Tech Publications Ltd, 2010, pp. 2511–2516. doi: 10.4028/www.scientific.net/MSF.638-642.2511.
- [10] D. Bernard, D. Gendron, J. M. Heintz, S. Bordère, and J. Etourneau, “First direct 3D visualisation of microstructural evolutions during sintering through X-ray computed microtomography,” *Acta Materialia*, vol. 53, no. 1, pp. 121–128, Jan. 2005, doi: 10.1016/j.actamat.2004.09.027.
- [11] J. Baruchel, J.-Y. Buffière, E. Maire, P. Merle, and G. Peix, “X-Ray tomography in material science,” *Hermès Science Publications*, 2000.

- [12] G. S. Upadhyaya, "Sintering Fundamentals," *Material Science Forum*, 2009, pp. 1-152.
- [13] H. E. Exner, "Stereology and 3D microscopy: useful alternatives or competitors in the quantitative analysis of microstructures?," *Image Analysis & Stereology*, vol. 23, pp. 73–82, 2004, doi: 0.5566/ias.v23.p73-82.
- [14] F. Xu, X. Hu, B. Lu, J. Zhao, X. Wu, and Q. Yuan, "Microstructures-evolution observation of boron carbide ceramic during sintering process by synchrotron radiation X-ray computed tomography," *Journal of Inorganic Materials*, vol. 24, pp. 175–181, 2009.
- [15] F. Xu, X. F. Hu, Y. Niu, J. H. Zhao, and Q. X. Yuan, "In situ observation of grain evolution in ceramic sintering by SR-CT technique," *Transactions of Nonferrous Metals Society of China*, vol. 19, Dec. 2009, doi: 10.1016/S1003-6326(10)60132-X.
- [16] F. Xu, X. F. Hu, H. Miao, and J. H. Zhao, "In situ investigation of ceramic sintering by synchrotron radiation X-ray computed tomography," *Optics and lasers in engineering*, vol. 48, no. 11, pp. 1082–1088, Nov. 2010, doi: 10.1016/j.optlaseng.2009.12.012.
- [17] J. Villanova, R. Daudin, P. Lhuissier, D. Jauffres, S. Lou, C. L. Martin, S. Labouré, R. Tucoulou, G. Martínez-Criado, and L. Salvo, "Fast in situ 3D nanoimaging: a new tool for dynamic characterization in materials science," *Materials Today*, vol. 20, no. 7, pp. 354–359, Sep. 2017, doi: 10.1016/j.mattod.2017.06.001.
- [18] J. Lesseur, "Imagerie 3D des matériaux et modélisations numériques : application aux multi-matériaux ferroélectriques," 2016. [Online]. Available: <https://theses.hal.science/tel-01281311>
- [19] G. Okuma, S. Watanabe, K. Shinobe, N. Nishiyama, A. Takeuchi, K. Uesugi, S. Tanaka, and F. Wakai, "3D multiscale-imaging of processing-induced defects formed during sintering of hierarchical powder packings," *Scientific reports*, vol. 9, no. 1, Dec. 2019, doi: 10.1038/s41598-019-48127-y.
- [20] Z. Yan, C. L. Martin, D. Bouvard, D. Jauffrès, P. Lhuissier, L. Salvo, L. Olmos, J. Villanova, and O. Guillon, "Coupling in-situ X-ray micro-and nano-tomography and discrete element method for investigating high temperature sintering of metal and ceramic powders," EPJ Web of Conferences, 2017, doi: 10.1051/epjconf/201714013006.
- [21] G. Okuma, N. Saito, K. Mizuno, Y. Iwazaki, R. Inoue, H. Kishi, A. Takeuchi, M. Uesugi, K. Uesugi, and F. Wakai, "Microstructural evolution of electrodes in sintering of multi-

layer ceramic capacitors (MLCC) observed by synchrotron X-ray nano-CT,” *Acta Materialia*, vol. 206, Mar. 2021, doi: 10.1016/j.actamat.2020.116605.

[22] A. M. Venkatesh, D. Bouvard, P. Lhuissier, and J. Villanova, “3D analysis of ceramic powder sintering by synchrotron X-ray nano-tomography,” *Journal of the European Ceramic Society*, vol. 43, no. 6, pp. 2553–2563, Jun. 2023, doi: 10.1016/j.jeurceramsoc.2022.12.065.

[23] S. Sakamoto, T. Kajino, T. Nasu, S. Sakaki, and Y. Sakatani, “New Technology and Application - Development of High Purity Alumina,” *Sumitomo Kagaku*, vol. 2020, 2020.

[24] R. Guinebretière, S. Arnaud, N. Blanc, N. Boudet, E. Thune, D. Babonneau, and O. Castelnau, “Full reciprocal-space mapping up to 2000 K under controlled atmosphere: the multipurpose QMAX furnace,” *Journal of Applied Crystallography*, vol. 53, no. 3, p. pp.650-661, 2020, doi: 10.1107/S160057672000432X.

[25] G. Martinez-Criado, J. Villanova, R. Tucoulou, D. Salomon, J. P. Suuronen, S. Labouré, C. Guilloud, V. Valls, R. Barrett, E. Gagliardini, and Y. Dabin, “ID16B: A hard X-ray nanoprobe beamline at the ESRF for nano-analysis,” *Journal of Synchrotron Radiation*, 2016, vol. 23, pp. 344–352. doi: 10.1107/S1600577515019839.

[26] S. C. Mayo, A. W. Stevenson, and S. W. Wilkins, “In-Line Phase-Contrast X-ray Imaging and Tomography for Materials Science,” *Materials*, vol. 5, no. 12, pp. 937–965, May 2012, doi: 10.3390/ma5050937.

[27] P. Cloetens, W. Ludwig, J. Baruchel, D. V. Dyck, J. V. Landuyt, J. P. Guigay, and M. Schlenker, “Holotomography: Quantitative phase tomography with micrometer resolution using hard synchrotron radiation x rays,” *Applied Physics Letters*, vol. 75, no. 19, pp. 2912–2914, Nov. 1999, doi: 10.1063/1.125225.

[28] A. Mirone, E. Brun, E. Gouillart, P. Tafforeau, and J. Kieffer, “The PyHST2 hybrid distributed code for high speed tomographic reconstruction with iterative reconstruction and a priori knowledge capabilities,” *Nuclear Instruments and Methods in Physics Research Section B: Beam Interactions with Materials and Atoms*, vol. 324, pp. 41–48, Apr. 2014, doi: 10.1016/j.nimb.2013.09.030.

[29] B. Münch, P. Trtik, F. Marone, and M. Stampanoni, “Stripe and ring artifact removal with combined wavelet - Fourier filtering,” *Optical Society of America*, vol. 17, no. 10, 2009, doi: 10.1364/oe.17.008567.

- [30] R. Kumar, “In situ nanotomography investigation of cavity nucleation and growth in light alloys during high temperature deformation,” 2019. [Online]. Available: <https://theses.hal.science/tel-02528824>.
- [31] S. Schlüter, A. Sheppard, K. Brown, and D. Wildenschild, “Image processing of multiphase images obtained via X-ray microtomography: A review,” *Water Resources Research*, vol. 50, no. 4, pp. 3615–3639, 2014, doi: 10.1002/2014WR015256.
- [32] A. Lyckegaard, G. Johnson, and P. Tafforeau, “Correction of ring artifacts in X-ray tomographic images,” *International Journal of Tomography and Statistics*, 18, pp.1-9, 2011.
- [33] O. Stamati, E. Andò, E. Roubin, R Cailletaud, M. Wiebicke, G. Pinzon , C. Couture, R. C. Hurley, R. Caulk, D. Caillerie, T. Matsushima, P. Besuelle, F. Bertoni, T. Arnaud, A. O. Laborin, R. Rorato, Y. Sun, A. Tengattini, O. Okubadejo, J-B. Colliat, M. Saadatfar, F. E Garcia, C. Papazoglou, I. Vego, S. Brisard, J. Dijkstra, G. Birmpilis, “spam: Software for Practical Analysis of Materials,” *Journal of Open Source Software*, no. 51, p. 2286, 2020, doi: 10.21105/joss.02286i.
- [34] “spam: Software for Practical Analysis of Materials, <https://tk.gricad-pages.univ-grenoble-alpes.fr/spam/index.html>,” 2020.
- [35] “Avizo 2021.1, <https://www.fei.com/software/avizo-formaterials-science>,” 2021.
- [36] A. Kornilov, I. Safonov, and I. Yakimchuk, “A Review of Watershed Implementations for Segmentation of Volumetric Images,” *Journal of Imaging*, vol. 8, no. 5. MDPI, May 01, 2022. doi: 10.3390/jimaging8050127.
- [37] H. E. Exner and C. Müller, “Particle rearrangement and pore space coarsening during solid-state sintering,” *Journal of the American Ceramic Society*, Jul. 2009, pp. 1384–1390. doi: 10.1111/j.1551-2916.2009.02978.x.
- [38] A. Wonisch, T. Kraft, M. Moseler, and H. Riedel, “Effect of different particle size distributions on solid-state sintering: A microscopic simulation approach,” *Journal of the American Ceramic Society*, Jul. 2009, pp. 1428–1434. doi: 10.1111/j.1551-2916.2009.03012.x.
- [39] L. Wang, V. Pouchly, K. Maca, Z. Shen, and Y. Xiong, “Intensive particle rearrangement in the early stage of spark plasma sintering process,” *Journal of Asian Ceramic Societies*, vol. 3, no. 2, pp. 183–187, Jun. 2015, doi: 10.1016/j.jascer.2015.02.004.

- [40] S. A. McDonald, C. Holzner, E. M. Lauridsen, P. Reischig, A. P. Merkle, and P. J. Withers, “Microstructural evolution during sintering of copper particles studied by laboratory diffraction contrast tomography (LabDCT),” *Scientific Reports*, vol. 7, no. 1, Dec. 2017, doi: 10.1038/s41598-017-04742-1.
- [41] J. Schindelin, I. Arganda-Carreras, E. Frise, V. Kaynig, M. Longair, T. Pietzsch, S. Preibisch, C. Rueden, S. Saalfeld, B. Schmid, and J. Y. Tinevez, “Fiji: An open-source platform for biological-image analysis,” *Nature Methods*, vol. 9, no. 7, pp. 676–682, Jul. 2012. doi: 10.1038/nmeth.2019.
- [42] “GrainFind handbook, in GeoDict 2022 User Guide from Math2Market GmbH, Germany,” doi: doi.org/10.30423/userguide.geodict2022, available at <https://www.geodict.com/userguide/geodict2022.html>.
- [43] “Porodict handbook, in GeoDict 2022 User Guide from Math2Market GmbH, Germany,” doi: doi.org/10.30423/userguide.geodict2022, available at <https://www.geodict.com/userguide/geodict2022.html>.
- [44] R. M. German, “Coarsening in sintering: Grain shape distribution, grain size distribution, and grain growth kinetics in solid-pore systems,” *Critical Reviews in Solid State and Materials Sciences*, vol. 35, no. 4, pp. 263–305, Oct. 2010, doi: 10.1080/10408436.2010.525197.
- [45] R. German, “Sintering: from empirical observations to scientific principles,” *Butterworth-Heinemann*, 2014.
- [46] W. C. Krumbein, “Measurement and geological significance of shape and roundness of sedimentary particles,” *Journal of Sedimentary Research*, vol. 11, no. 2, 1941, pp. 64–72.
- [47] J. Ohser and F. Mücklich, “Statistical Analysis of Microstructures in Materials Science”, *Wiley and sons*, 2000.
- [48] R. L. Coble, “Sintering crystalline solids. I. intermediate and final state diffusion models,” *Journal of Applied Physics*, vol. 32, no. 5, pp. 787–792, 1961, doi: 10.1063/1.1736107.
- [49] G. C. Kuczynski, “Study of the sintering of glass,” *Journal of Physics*, 20:1160–1163, 1949.

- [50] W. D. Kingery and M. Berg, "Study of the initial stage of sintering solids by viscous flow, evaporation-condensation, and self-diffusion," *Journal of Applied Physics*, 21:1205–1212, 1955.
- [51] R. L. Coble, "Initial Sintering of Alumina and Hematite," *Journal of the American Ceramic Society*, vol. 41, no. 2, pp. 55–62, 1958, doi: 10.1111/j.1151-2916.1958.tb13519.x.
- [52] D. L. Johnson and I. B. Cutler, "Diffusion Sintering: I, Initial Stage Sintering Models and Their Application to Shrinkage of Powder Compacts," *Journal of the American Ceramic Society*, vol. 46, no. 11, pp. 541–545, 1963, doi: 10.1111/j.1151-2916.1963.tb14606.x.
- [53] J. J. Koenderink and A. J. van Doorn, "Surface shape and curvature scales," *Image and vision computing*, 10(8), pp.557-564, 1992.
- [54] H. H. Hu, H. Y. Chen, C. I. Hung, W. Y. Guo, and Y. T. Wu, "Shape and curvedness analysis of brain morphology using human fetal magnetic resonance images in utero," *Brain Structure and Function*, vol. 218, no. 6, pp. 1451–1462, Nov. 2013, doi: 10.1007/s00429-012-0469-3.
- [55] A. J. Shahani, E. B. Gulsoy, V. J. Roussochatzakis, J. W. Gibbs, J. L. Fife, and P. W. Voorhees, "The dynamics of coarsening in highly anisotropic systems: Si particles in Al-Si liquids," *Acta Materialia*, vol. 97, pp. 325–337, Jul. 2015, doi: 10.1016/j.actamat.2015.06.064.
- [56] B. Paredes-Goyes, D. Jauffres, J. M. Missiaen, and C. L. Martin, "Grain growth in sintering: A discrete element model on large packings," *Acta Materialia*, vol. 218, Oct. 2021, doi: 10.1016/j.actamat.2021.117182.
- [57] A. Burr, P. Lhuissier, C. L. Martin, and A. Philip, "In situ X-ray tomography densification of firn: The role of mechanics and diffusion processes," *Acta Materialia*, vol. 167, pp. 210–220, Apr. 2019, doi: 10.1016/j.actamat.2019.01.053.